8-9-2011

Predicted Velocity and Density Structure of the Exhuming Papua New Guinea Ultrahigh-Pressure Terrane

Sarah J. Brownlee
University of California - Santa Barbara, sarah.brownlee@wayne.edu

Bradley R. Hacker
University of California - Santa Barbara, hacker@geol.ucsb.edu

Matthew Salisbury
Bedford Institute of Oceanography

Gareth Seward
University of California - Santa Barbara, seward@geol.ucsb.edu

Timothy A. Little
Victoria University of Wellington, tim.little@vuw.ac.nz

See next page for additional authors

Authors
Sarah J. Brownlee, Bradley R. Hacker, Matthew Salisbury, Gareth Seward, Timothy A. Little, Suzanne A. Baldwin, and Geoffrey A. Abers

Predicted velocity and density structure of the exhuming Papua New Guinea ultrahigh-pressure terrane

Sarah J. Brownlee,[1] Bradley R. Hacker,[1] Matthew Salisbury,[2] Gareth Seward,[3] Timothy A. Little,[4] Suzanne L. Baldwin,[5] and Geoffrey A. Abers[6]

Received 4 January 2011; revised 22 April 2011; accepted 5 May 2011; published 9 August 2011.

[1] New electron backscatter diffraction measurements show that the Papua New Guinea (PNG) ultrahigh-pressure (UHP) terrane is dominated by rocks with weakly oriented quartz and feldspar and less abundant strongly oriented hornblende, clinopyroxene, and mica. Velocities measured at high pressures (600 MPa) show that V_P is 5.8–6.3 km/s for gneiss samples, 6.5–7.7 km/s for amphibolite, and 7.7–8.2 km/s for eclogite and V_S is 3.4–3.9 km/s for gneiss, 4.0–4.4 km/s for amphibolite, and 4.5–4.6 km/s for eclogite. Velocities and anisotropies calculated from mineral crystal preferred orientations (CPOs) are equivalent to within 5% of the measured values. The highest seismic anisotropy for the PNG terrane is in amphibolite at 8% and 7% for V_P and V_S, respectively. Calculations of seismic velocities at depth based on predicted mineral assemblages indicate that the exhuming UHP terrane is of dominantly mafic composition below ~20 km depth. Anisotropy in the PNG terrane is expected to be quite low and is controlled by the orientation of the foliation. If observable, changes in anisotropy across the exhuming body may be used to differentiate among the different proposed mechanisms of UHP exhumation.

Citation: Brownlee, S. J., B. R. Hacker, M. Salisbury, G. Seward, T. A. Little, S. L. Baldwin, and G. A. Abers (2011), Predicted velocity and density structure of the exhuming Papua New Guinea ultrahigh-pressure terrane, *J. Geophys. Res.*, *116*, B08206, doi:10.1029/2011JB008195.

1. Introduction

[2] Understanding how giant ultrahigh-pressure (UHP) terranes are exhumed [*Hacker and Peacock*, 1995] has been a principal scientific goal ever since such terranes were discovered [*Chopin*, 1984; *Wang et al.*, 1989]. Much has been learned from UHP terranes in ancient orogenic belts [e.g., *Hacker et al.*, 2000, 2010] because of our ability to examine exposures of formerly deeply buried rocks in detail. The UHP terrane in the D'Entrecasteaux Islands of Papua New Guinea [*Baldwin et al.*, 2004] is *actively* exhuming [*Little et al.*, 2011], however, affording the opportunity to use geophysical imaging, particularly seismology, to learn about ongoing geodynamic processes. At present, this makes the UHP terrane in PNG unique and therefore worthy of intensive study. The purpose of this paper is to "ground truth" geophysical observations in the region by (1) measuring in the laboratory the seismic velocities and densities of a representative group of rocks from the Papuan UHP terrane, (2) calculating the seismic velocities and densities of the same rocks from mineralogical data collected by electron backscatter diffraction (EBSD), and (3) modeling the velocity and density structure of the exhuming PNG UHP terrane at depth.

1.1. D'Entrecasteaux Islands

[3] The D'Entrecasteaux Islands ultrahigh-pressure terrane in Papua New Guinea, like most UHP terranes, consists dominantly of quartzofeldspathic gneiss with 5–10% mafic and minor ultramafic blocks of chiefly meter to decameter scale [*Baldwin et al.*, 2008; *Little et al.*, 2011]. Much of the mafic material is amphibolite, but variably retrogressed eclogite is widely distributed. Metamorphic conditions during the peak of subduction reached ~700–750°C and >3.0–3.6 GPa, based on mineral compositions from a coesite-bearing eclogite [*Davies and Warren*, 1992; *Monteleone et al.*, 2007; *Baldwin et al.*, 2008]. The exhumation path is partly constrained by amphibolite-facies metamorphic overprinting at pressures of ~1 GPa down to 0.5 GPa at maximum temperatures of 700°C [*Hill and Baldwin*, 1993]. Unusual for a UHP terrane, the D'Entrecasteaux Islands quartzofeldspathic gneisses and eclogites are intruded by

[1]Earth Research Institute, University of California, Santa Barbara, California, USA.
[2]Geological Survey of Canada-Atlantic, Bedford Institute of Oceanography, Dartmouth, Nova Scotia, Canada.
[3]Department of Earth Science, University of California, Santa Barbara, California, USA.
[4]Department of Earth Sciences, Victoria University of Wellington, Wellington, New Zealand.
[5]Department of Earth Sciences, Syracuse University, Syracuse, New York, USA.
[6]Lamont-Doherty Earth Observatory, Columbia University, Palisades, New York, USA.

0148-0227/11/2011JB008195

Table 1. Sample Descriptions

Sample	Description
PNG/08-02	Equigranular plagioclase-quartz-biotite gneiss (quartzofeldspathic gneiss) with minor K-feldspar, muscovite and clinozoisite. Muscovite and biotite are both coarse and unaltered, except for 1% chloritization of biotite. Zoisite and K-feldspar are xenoblastic and likely resorbed. Interpretation: the peak-P mineral assemblage is K-white mica + biotite ± plagioclase + K-feldspar + clinozoisite + quartz/coesite; the retrograde assemblage is the same, but without clinozoisite and K-feldspar. Average grain size ~0.5–1 mm. UTM location 56L 0197368 8950410.
PNG/08-10	Equigranular clinopyroxene–garnet–phengite–quartz gneiss (eclogite) with minor hornblende, zoisite, apatite, and rutile. Hornblende occurs in two habits: a coarse matrix phase and a fine-grained (~1–5 μm) symplectite (~2–4 vol % of rock) with plagioclase formed from the decomposition of clinopyroxene. Omphacite is 2–4 vol % decomposed to hornblende + plagioclase. Garnet and rutile are unaltered. Phengite is 1–2 vol % decomposed to biotite + plagioclase symplectite. This rock contains coesite [*Baldwin et al.*, 2008]. Interpretation: peak P assemblage is garnet + omphacite + clinozoisite + phengite + coesite + rutile. Average grain size ~0.5–1 mm. UTM location 56L 0221381 8950186.
PNG/08-17	Equigranular hornblende–plagioclase–quartz–clinozoisite gneiss (amphibolite) with minor garnet, sphene, apatite and rutile. Rutile is present as coarse, gemmy grains. Sphene is present as gemmy inclusions in garnet and hornblende and as rims on some of the rutile. Oriented plagioclase/quartz inclusions in hornblende suggest that the hornblende may have been derived from clinopyroxene. Zoisite is ~5 vol % replaced by plagioclase and there is ~2 vol % red material (probably FeOOH) in cracks. Interpretation: peak P assemblage is garnet + hornblende ± clinopyroxene + clinozoisite ± plagioclase + quartz/coesite + rutile, perhaps overgrowing prograde sphene; overprinting assemblage is garnet + hornblende + plagioclase + quartz + sphene. Average grain size ~0.25–0.5 mm. UTM location 100 m below 56L 0218907 8961334 (dense jungle).
PNG/08-33	Equigranular plagioclase–quartz–muscovite gneiss (quartzofeldspathic gneiss) with minor K-feldspar, garnet, biotite and zoisite and a trace of kyanite. Garnet is xenoblastic, suggesting resorption, and is altered to biotite along cracks. Zoisite is elongate and intergrown with K-white mica. 3–6 vol % of K-white mica is altered to biotite, which is exclusively a retrograde phase. Kyanite is present as inclusions in garnet. Interpretation: peak P assemblage is garnet + K-white mica + clinozoisite + kyanite ± plagioclase + K-feldspar + quartz/coesite; overprinting assemblage is plagioclase + biotite + quartz. Average grain size ~0.5–1 mm. UTM location 56L 0219609 8953892.
PNG/08-43	Inequigranular plagioclase–quartz–biotite–hornblende–garnet gneiss (quartzofeldspathic gneiss) with minor K-feldspar, clinozoisite, rutile. Biotite has two habits: coarse, equant grains and a fine (5–20 μm) symplectite (15–20 vol % of biotite) with plagioclase formed from the decomposition of K-white mica. Hornblende is coarse grained, includes garnet, and is both wrapped by the foliation and cuts across the foliation. Garnet is xenoblastic, suggesting resorption, and is altered to ~10–15 vol % green biotite along cracks. Zoisite is xenoblastic and altered to biotite. Rutile has thin rims of sphene. Interpretation: peak P assemblage is garnet + hornblende + K-white mica + clinozoisite ± biotite + K-feldspar ± plagioclase + rutile + quartz/coesite; overprinting assemblage is plagioclase + biotite + sphene + quartz. Average grain size ~0.5–1.5 mm. UTM location 56L 0256055 89596.
PNG/08-44	Equigranular hornblende–clinozoisite–clinopyroxene–garnet gneiss (garnet–clinopyroxene amphibolite), with minor K-white mica, rutile, sphene and calcite. The clinopyroxene is 2–4% decomposed into a fine grained (1–2 μm) diopside + plagioclase symplectite, the K-white mica is extensively altered to a biotite + plagioclase symplectite that comprises 30–35 vol % of the sample. Sphene is present as inclusions in garnet and hornblende and as rims on some of the rutile. Interpretation: peak P assemblage is hornblende + clinozoisite + clinopyroxene + garnet + phengite + rutile; overprinting assemblage is hornblende + diopside + clinozoisite + garnet + biotite + sphene. Average grain size ~0.5–1 mm. UTM location 56L 0256170 89529.

~30–40 vol % granodiorite (*sensu lato*) in tens to hundred km^2 plutons and dikes [*Hill and Baldwin*, 1993]. The granodiorite includes leucogranites and is more leucocratic than the host quartzofeldspathic gneiss. The bulk of the quartzofeldspathic gneiss and eclogites have a gently dipping foliation and gently plunging E–W lineation formed at amphibolite-facies conditions [*Hill*, 1994; *Little et al.*, 2011]. At the highest structural levels, near the tops of the domes, this fabric crenulates an older, steeply dipping foliation.

1.2. Sample Locations, Mineralogy, and Microstructure

[4] Representative, oriented samples (~5 kg each) were collected from six locations (Table 1 and Figure 1). Three samples (PNG/08-02, PNG/08-33, and PNG/08-43) are of the dominant quartzofeldspathic gneiss (Figure 2) with moderately developed foliation defined by biotite. Sample PNG/08-17 is a typical hornblende–plagioclase amphibolite, and sample PNG/08-44 is a much less common garnet amphibolite. The amphibolite samples have a moderate- to well-developed foliation and lineation defined by hornblende. Sample PNG/08-10 is from the coesite-bearing eclogite of *Baldwin et al.* [2008]. The eclogite has a moderately developed foliation and lineation defined by pyroxene.

2. Methods

2.1. Velocity Measurements

[5] High-pressure velocity measurements were made at the Dalhousie University–Geological Survey of Canada High-Pressure Laboratory. Three orthogonal ~2.5 cm diameter and ~7.5 cm long cores were cut from each sample. The X core is parallel to the foliation and lineation, the Y core is parallel to the foliation and perpendicular to the lineation, and the Z core is perpendicular to the foliation. V_P and V_S were measured isothermally using the pulse transmission technique in a hydrostatic pressure vessel at increasing pressure intervals from 0 to 600 MPa [e.g., *Birch*, 1960; *Christensen*, 1965]. Both V_{S1} and V_{S2} were measured for the X and Y cores, whereas only one V_S measurement was made in the Z cores.

2.2. Electron Backscatter Diffraction and Mineral Modes

[6] High-pressure laboratory velocity measurements allow accurate characterization of rock velocities, but also have

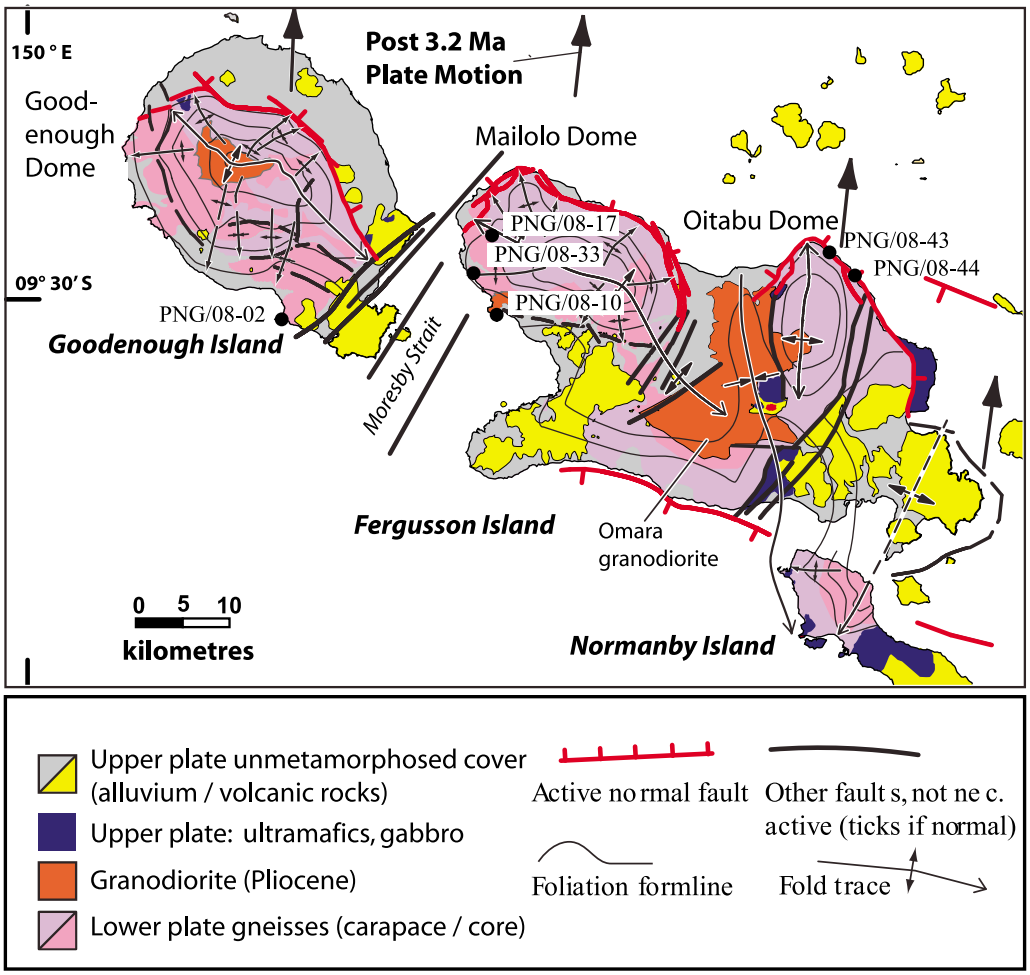

Figure 1. Generalized geologic map of the Papua New Guinea ultrahigh-pressure terrane after *Little et al.* [2011]. Black dots indicate sample locations for this study.

some disadvantages. For example, the three cores from each sample are not exactly the same, some of the samples were partially altered, the application of pressure is required to close cracks, and the velocity extrema cannot be measured except fortuitously [*Godfrey et al.*, 2000]. For these reasons, and others, it is advantageous to also calculate velocities using electron backscatter diffraction (EBSD). With EBSD, the mineral orientations are measured and mapped at the micron scale, and the 3D seismic properties of the rock are calculated from the elastic constants (C_{ij}), densities, and orientations of the constituent minerals [e.g., *Mainprice*, 1990]. The advantages of using EBSD measurements to calculate seismic properties include the ability to measure the complete CPO in a single thin section. These data, in conjunction with mode fraction data for the constituent mineral phases (see below), allow one to calculate the V_P, V_{S1}, and V_{S2} in all directions, and to directly relate velocity anisotropy to mineralogy and microstructure (e.g., the foliation and lineation). Application of this method is limited only by the availability of samples and appropriate C_{ij}.

[7] Thin sections were cut from each of the 3 cores so that the surface of the thin section was perpendicular to the foliation, and the foliation was either parallel (X section), or perpendicular (Y and Z sections) to the long axis of the thin section. In one sample, PNG/08-43, the X core thin section was cut parallel to the foliation. The thin sections were mechanically polished down to 0.25 μm using diamond grit, and further polished in 50 nm colloidal silica for up to 8 h. They were then coated with ~6 nm of carbon to prevent charging. EBSD measurements were done at UCSB in an FEI Quanta 400f scanning electron microscope with a field emission gun, an Oxford Instruments EBSD camera, and HKL Channel 5 software. Patterns were collected with the sample inclined at 20° to the beam, using an accelerating voltage of 20 kV, and a spot size of ~1 μm. EBSD maps were collected by moving the stage from point to point rather than by beam scanning to allow for reindexing of saved diffraction patterns; each point is spaced ~200–300 μm, resulting in a scanned area of ~100–300 mm^2 for each thin section. Energy dispersive X-ray spectra (EDS) were collected simultaneously using an Oxford Instruments INCAx-act detector (model 51-ADD0055) using ~0.1 keV window widths. Because the Oxford system is unable to use on-the-fly EDS data to aid in indexing of diffraction patterns, it misidentifies a large percentage (up to ~10%) of the crystals. To surmount this difficulty and ensure proper

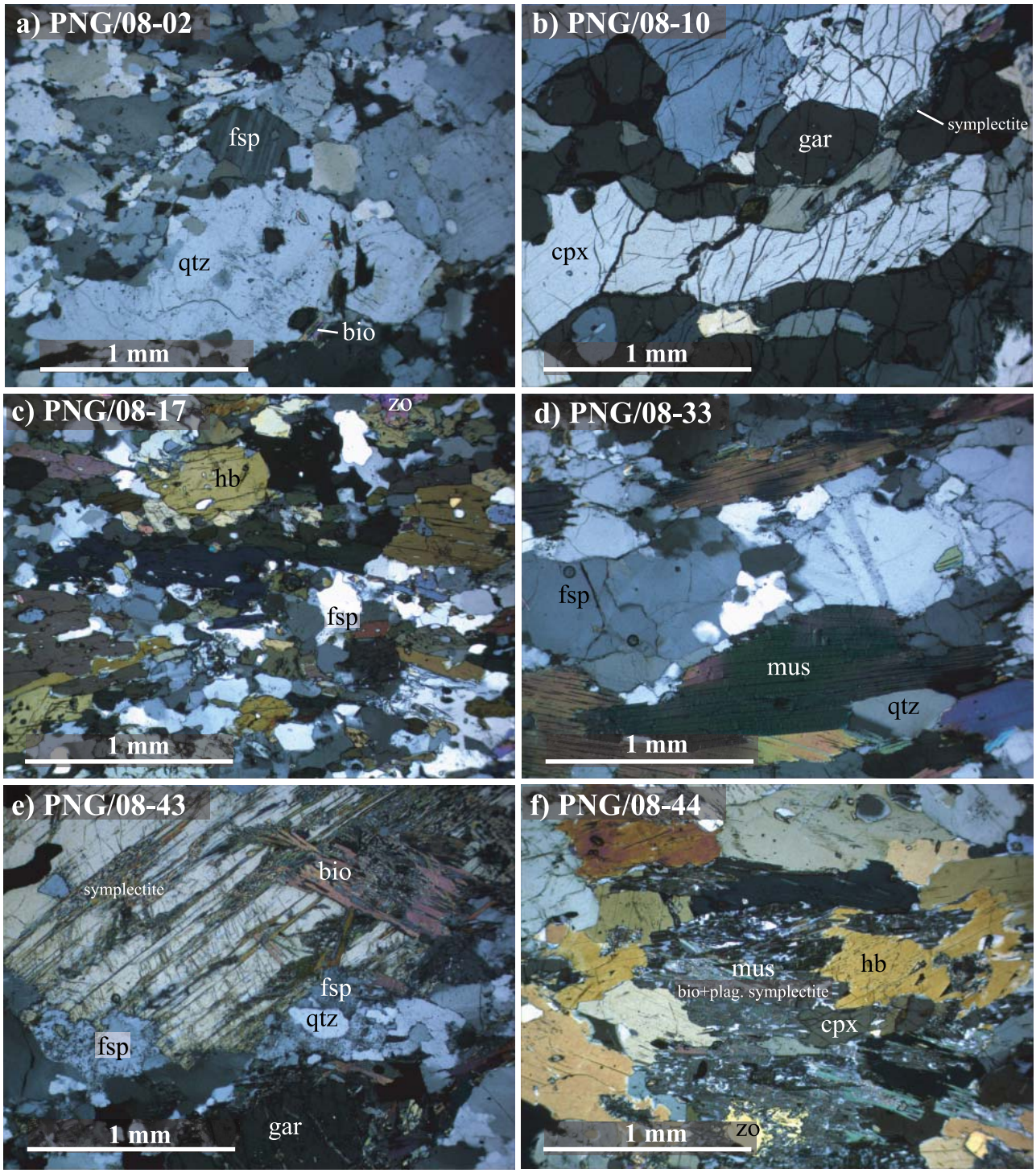

Figure 2. Photomicrographs of the PNG samples in crossed polarized light at 5× magnification. All images are taken from thin sections cut perpendicular to the foliation and with the foliation approximately horizontal in the image. Horizontal field of view is ~2.5 mm.

indexing, the EBSD patterns were all reindexed in conjunction with the EDS data after data collection, using an in-house MATLAB code, which assigns phases based on a root-mean-square fit to reference EDS data for each phase present. The EBSD patterns are then reindexed using only the assigned phase. Mineral modes (Table 2) would ideally be determined directly from EDS data, but the Oxford software for simultaneous EDS data collection requires saving EDS counts in at most 15 specified element windows, and is therefore ill suited to distinguishing similar phases (e.g., muscovite and K-feldspar). Point counting of

Table 2. Average Modal Compositions (±Standard Deviation) Based on EDS Data Collected Simultaneously With EBSD Measurements and Point Counting[a]

	Modal Compositions (vol %)								
	qtz	fsp	mus	bio	hbl	cpx	gar	czo	rut
PNG/08-02	30.5 ± 3.1	65.4 ± 2.7		3.8 ± 0.8				0.3 ± 0.1	
PNG/08-10	5.7 ± 1.8		1.1 ± 0.2			53.5 ± 5.0	37.7 ± 3.4	0.2 ± 0.1	1.8 ± 0.3
PNG/08-17	11.6 ± 5.0	20.2 ± 2.5			56.9 ± 5.1		0.3 ± 0.1	10.9 ± 2.7	0.1 ± 0.1
PNG/08-33	31.2 ± 2.5	58.6 ± 2.7	6.1 ± 0.6	3.4 ± 3.1			0.6 ± 0.4		
PNG/08-43	36.0 ± 3.0	45.4 ± 4.5		9.9 ± 1.5	6.1 ± 2.1		2.5 ± 1.5		
PNG/08-44			1.0 ± 1.7		61.5 ± 1.7	15.5 ± 1.1	3.9 ± 0.4	18.0 ± 1.3	0.1 ± 0.1

[a]Mineral abbreviations are after *Kretz* [1983].

thin sections was used in conjunction with the EDS data to resolve such ambiguities.

2.3. Velocity Calculations

[8] Seismic velocities were calculated from EBSD measurements and mineral modes using software written by David Mainprice, which follows the method described by *Mainprice* [1990]. For each thin section, every EBSD data point is used in the velocity calculation, including multiple measurements from the same grain. Voigt–Reuss–Hill (VRH) averaging is used first to average the measurements of each phase, and then to combine the phases according to their measured modal proportions. Elastic constants, C_{ij}, and densities were taken from the literature (Table 3) and, when necessary, were rotated to the same crystallographic reference frame as the EBSD data.

3. Results

3.1. Crystal Preferred Orientations

[9] The crystal preferred orientations (CPOs) are shown as pole figures of 1 point-per-grain measurements in Figures 3 and 4. The X, Y, and Z thin sections for each rock yield similar CPO data when rotated to the same sample reference frame. The weakest CPOs (lowest MUD and M index values) are measured for quartz and plagioclase in the quartzofeldspathic gneisses (Figure 3). The strongest CPOs (highest MUD and M index values) are measured for clinozoisite and hornblende in the amphibolite samples (Figure 4).

[10] Quartz and plagioclase in all samples have weak CPOs (Figure 3). The common slip directions in quartz, [c] and ⟨a⟩, are not preferentially aligned with the lineation, and the common slip planes in quartz, e.g., {m}, {r}, or {z} [*Lister*, 1979; *Linker et al.*, 1984], are not preferentially aligned with the foliation. PNG/08-10X shows a slight alignment of quartz [c] with lineation; however, only 98 grains were measured. PNG/08-33X displays a CPO that may be consistent with prism ⟨a⟩ slip. The plagioclase CPOs are comparable in strength to the quartz CPOs, and are different for each sample.

[11] Although only two samples have significant amounts of hornblende, the hornblende CPOs are strong, and the most consistent between samples (Figure 4). The [001] directions are ~parallel to the lineation, and (100) is ~parallel to the foliation, implying that [001](100) was the dominant slip system, as expected [*Hacker and Christie*, 1990].

[12] Clinozoisite also has a consistently strong CPO and the highest M index values (Figure 4). [010] is ~parallel to the lineation in both samples that have significant clinozoisite. (001) is ~parallel to the foliation in sample PNG/08-44, and both (001) and (100) are approximately parallel to the foliation in sample PNG/08-17. The probable slip systems are thus [010](001) and [010]{h01}.

[13] Clinopyroxene also exhibits a relatively strong CPO (Figure 4). [001] is approximately parallel to the lineation in both samples. (010) is ~parallel to the foliation in both samples, with a subsidiary maximum of (100) parallel to foliation in sample 10. The dominant slip system was likely [001](010), with minor slip on [001](100). Slip on [001](100) has commonly been inferred for omphacite [*Bascou et al.*, 2002; *Le Roux et al.*, 2008]. *Bascou et al.* [2002] conclude that slip on {110} planes is also involved in the aligning of (010) parallel to the flow plane.

[14] Only a few tens of mica grains were indexed in each sample due to their relative scarcity in samples analyzed and because they do not polish well. The micas are consistently oriented with (001) parallel to the foliation (Figure 4); as expected for mica there is no preferred orientation of [hk0] directions with respect to lineation [*Lloyd et al.*, 2009].

Table 3. Sources of C_{ij} for Each Mineral in Velocity Calculations

Mineral	C_{ij}	C_{ij} Source
Quartz	Quartz at 20°C	*Lakshtanov et al.* [2007]
Feldspar	Plagioclase (an_{24})	*Ryzhova* [1964]
Biotite	Biotite	*Aleksandrov and Ryzhova* [1961]
Muscovite	Muscovite	*Vaughan and Guggenheim* [1986]
Hornblende	Hornblende	*Aleksandrov and Ryzhova* [1961]
Clinopyroxene in eclogite	Omphacite ($di_{34}jd_{66}$)	*Bhagat et al.* [1992]
Clinopyroxene in amphibolite	Diopside ($di_{72}he_{09}jd_{03}Cr_{03}ts_{12}$)	*Collins and Brown* [1998]
Garnet	Almandine	
($Alm_{74}Py_{20}Gr_3Sp_3$)	*Soga* [1967]	
Clinozoisite	Zoisite	*Mao et al.* [2007]
Rutile	Rutile	*Bass* [1995]

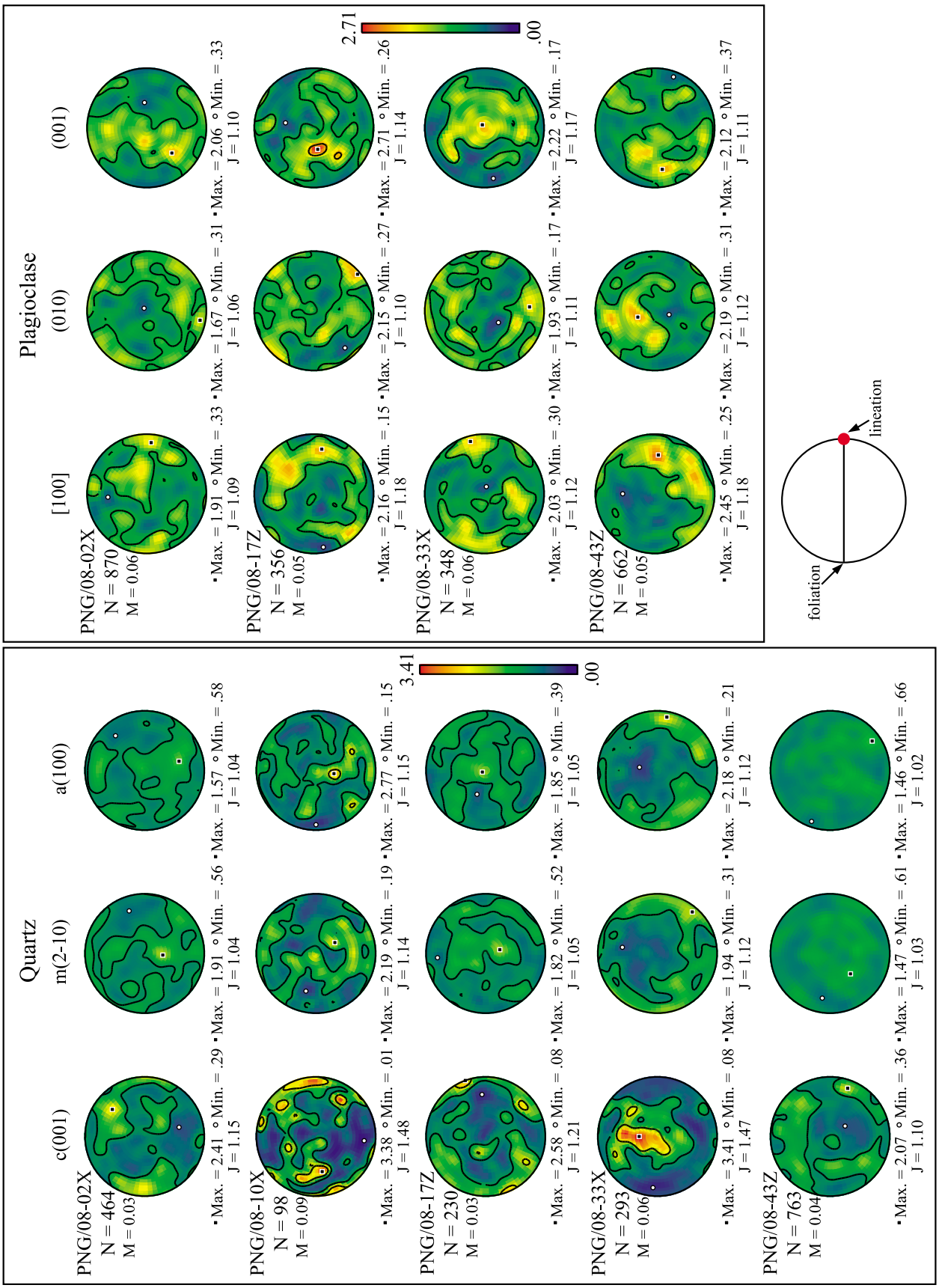

Figure 3. Equal-area lower hemisphere pole figures for quartz and plagioclase. Shading scale is linear in multiples of uniform distribution (MUD), and contour intervals are 1 MUD.

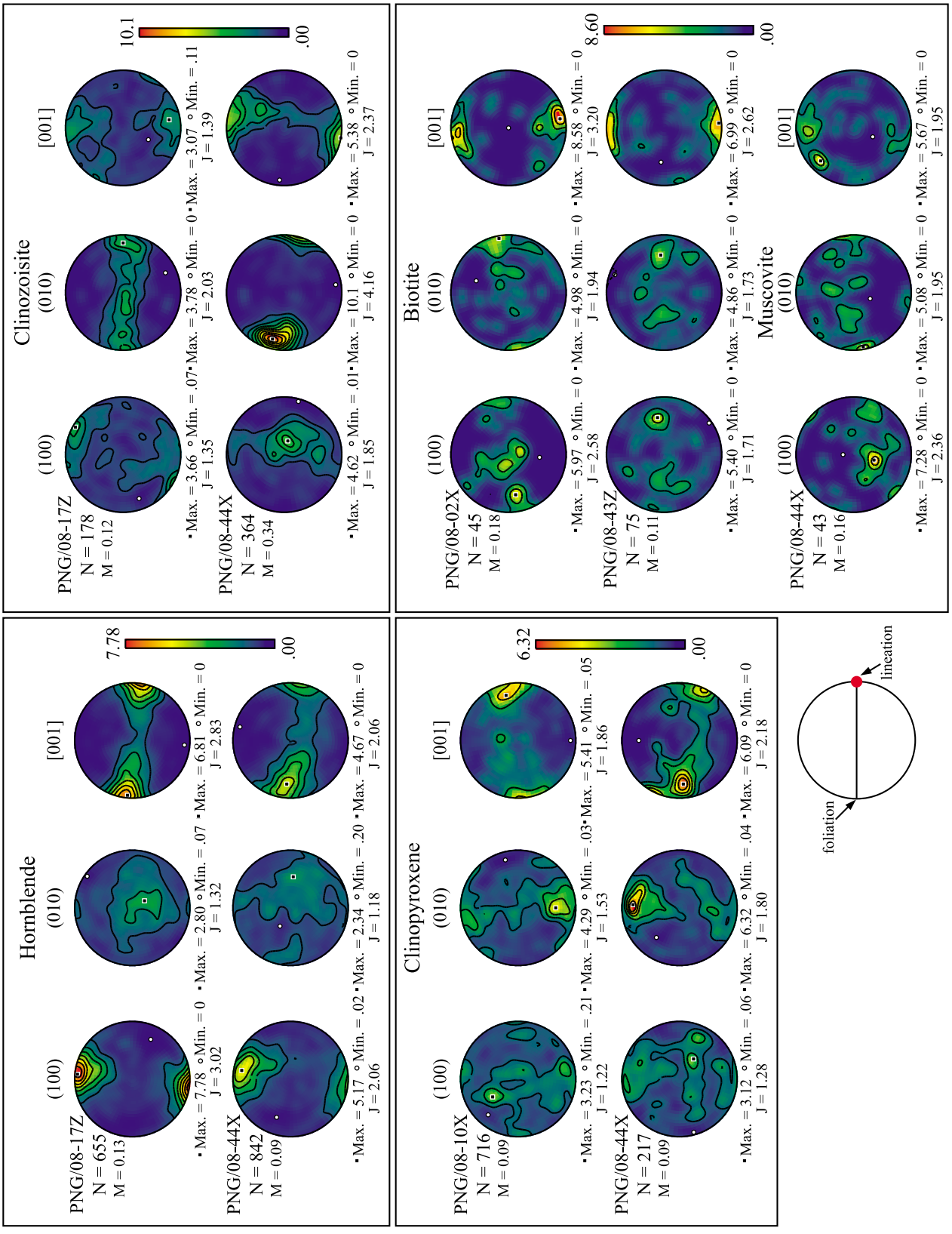

Figure 4. Equal-area lower hemisphere pole figures for hornblende, clinozoisite, clinopyroxene, and biotite/muscovite. Shading is linear in MUD, and contour intervals are 1 MUD, except for biotite/muscovite, which are 2 MUD.

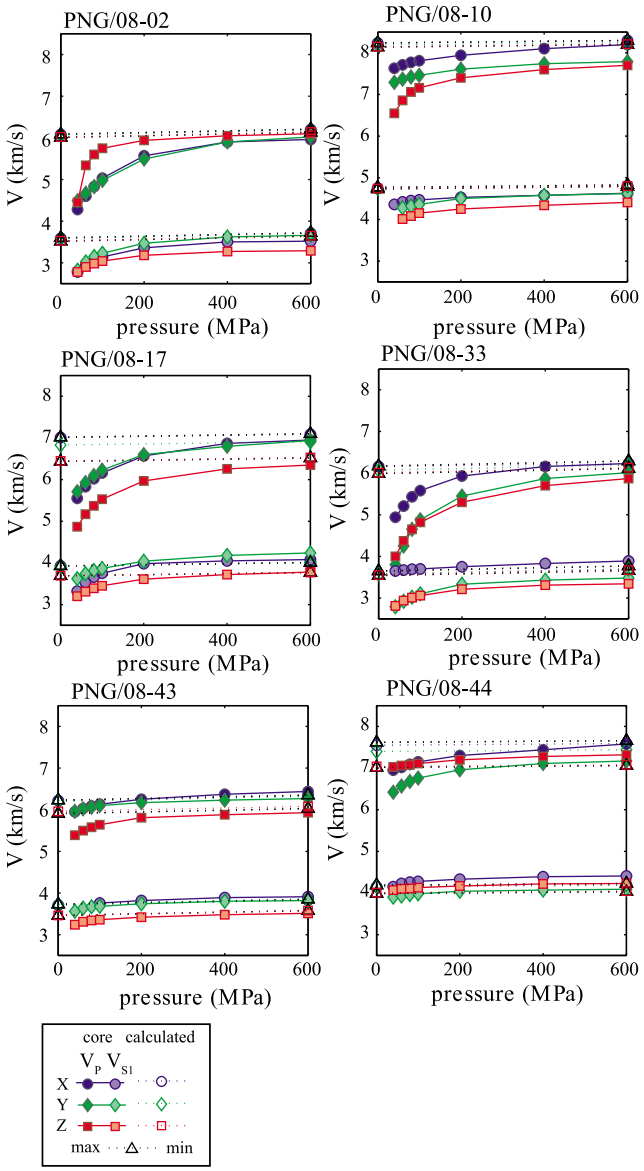

Figure 5. V_P and V_{S1} measured for the X (solid circles), Y (solid diamonds), and Z (solid squares) cores from each sample. The calculated V_P and V_{S1} corresponding to the direction of each core measurement are shown as the corresponding open symbol at 0 MPa. Calculated V_P and V_{S1} maximum and minimum are shown as open triangles at 0 MPa, and all calculated values are extrapolated to 600 MPa using the theoretical $\partial V/\partial P$ calculated for the bulk composition of each sample using the method of *Hacker and Abers* [2004].

3.2. Velocity Measurements and Calculations

[15] The high pressure seismic velocity measurements are shown in Figures 5 and 6. The measured velocities are a function of pressure and are presumed to approach the intrinsic velocity with increasing confining pressure as fractures close [cf. *Christensen*, 1965]. The highest P wave velocities were measured in the X cores (parallel to foliation and lineation), and the lowest were measured in the Z cores (perpendicular to foliation), except in sample PNG/08-02, in which the Z core yielded the highest velocity.

[16] Seismic velocities were calculated from the EBSD data obtained from each of the 3 orthogonal cores of each sample, rotated into the same sample reference frame, and then combined using a VRH average (Table 4). The calculated velocities for directions corresponding to the X, Y, and Z cores are shown in Figure 5 as open symbols; values are shown for STP and extrapolated to higher pressures using the isotropic $\partial V_P/\partial P$ and $\partial V_S/\partial P$ calculated for each rock using the mineral properties and equation of state from *Hacker and Abers* [2004] updated to 2010. The measured and calculated velocities agree to within 2% for some samples (e.g., samples PNG/08-02 and PNG/08-17) and disagree by as much as 6% (sample PNG/08-10). These differences may be the result of (1) the incomplete closure of cracks during the laboratory velocity measurements, (2) the presence of fine-grained alteration phases that were not measured in the EBSD analyses, (3) deficiencies in the C_{ij} for the relevant minerals, or (4) deficiencies in the calculated $\partial V_P/\partial P$ or $\partial V_S/\partial P$ (e.g., samples PNG/08-33 and PNG/08-44).

[17] The maximum calculated V_p ranges from 6.1 to 8.2 km/s. The calculated P wave velocities, both at STP and extrapolated to 600 MPa, for the X directions of all samples are within 0.23 km/s (3.5%) of the measured values at 600 MPa. The calculated V_P in the Y and Z directions are within 0.28 km/s (4.8%) for all samples except PNG/08-10, for which the calculated minimum V_p at STP is much higher (+0.45 km/s or 5.9%) than measured. The most probable explanation for this is that the calculated velocities do not account for the elastic effects of the micron-scale symplectites that comprise 2–4% of the sample. The plagioclase in the symplectite will lower the measured velocity relative to the calculated velocity. This highlights the ability of EBSD-based velocity calculations to exclude the effects of alteration. There are only two cases where the measured velocity from a core at 600 MPa is measurably greater (>0.1 km/s) than the calculated velocity at STP in that direction, the PNG/08-43 X core and the PNG/08-44 Z core (Table 4); both of these samples have extensive alteration.

[18] The measured V_P anisotropy, which is defined as the difference between maximum and minimum V_P divided by the median of V_P, $(V_{Pmax} - V_{Pmin})/((V_{Pmax} + V_{Pmin})/2)*100$, is also a function of pressure and is most accurate at high pressures when most cracks are closed (Figure 6). The calculated V_p anisotropy is 5.3–8.6% in samples that contain hornblende, and 1.3–3.1% in samples without hornblende. V_{S1} ranges from 3.5 to 4.8 km/s; the maximum calculated shear wave anisotropy, which is defined as the difference between V_{S1} and V_{S2} in a given propagation direction divided by the median of V_{S1}, $(V_{S1i} - V_{S2i})/((V_{S1max} + V_{S1min})/2)*100$ for propagation direction i, range from 5.5 to 7.0% in samples containing hornblende, and from 1.2 to 3.5% in samples without hornblende; this is consistent with results of *Tatham et al.* [2008], who suggested amphibole as a principal contributor to seismic anisotropy. Calculated V_S anisotropies in the X and Y directions agree to within 5% of the measured values. V_S anisotropy was not measured in the Z direction because only one V_S measurement was made on the Z cores due to difficulty in identifying the lineation in the Z core orientation. The calculated V_p anisotropies are

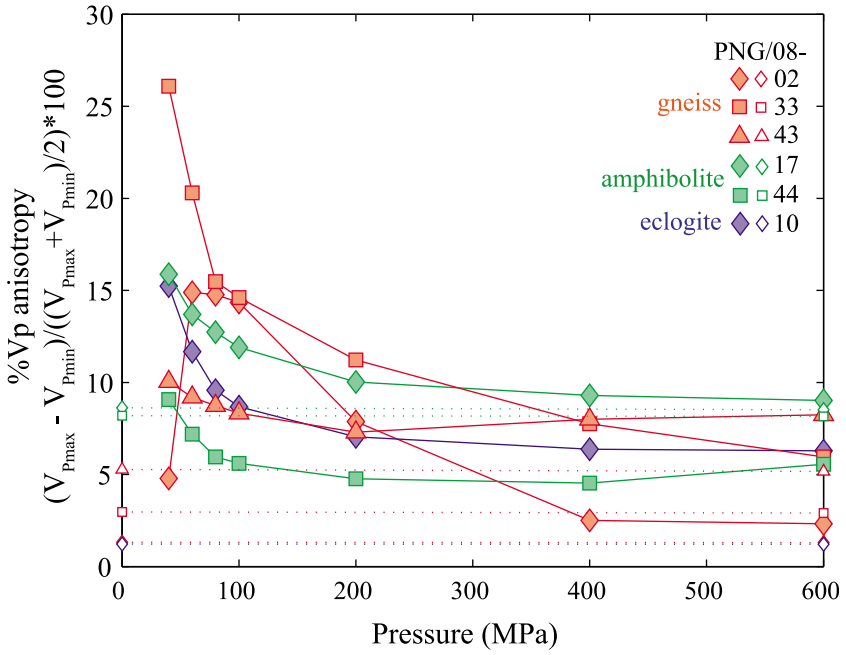

Figure 6. Percent V_P anisotropy from core measurements at each pressure step (solid symbols), and calculated from EBSD data (open symbols). The calculated values at 600 MPa are calculated from the extrapolated Vp using the $\partial V_P/\partial P$ given by *Hacker and Abers* [2004] for each rock composition.

lower than those measured by 0.9–5.0%, except for PNG/08-44, for which the calculated anisotropy is 2.7% higher.

[19] Figure 7 shows the calculated velocities in 3D using equal-angle lower hemisphere stereonets. The amphibolites, PNG/08-17 and PNG/08-44, are the most anisotropic and the quartzofeldspathic gneisses and eclogite are the least. The velocity anisotropy for four of the samples has approximately uniaxial symmetry, with a unique slow direction perpendicular to the foliation. Samples PNG/08-10 and PNG/08-33 are roughly orthorhombic: anisotropy within the foliation plane accounts for 30% and 60% of the total anisotropy, respectively. All of the samples have their slowest V_P direction subperpendicular to the foliation, and their fastest V_p direction subparallel to the lineation.

[20] The highest shear wave anisotropies are for waves propagating parallel to the foliation, except for samples PNG/08-10 and PNG/08-33, which have weak and more irregular V_s anisotropy. For these propagation directions the fast S wave polarization plane is parallel to the foliation. For waves propagating perpendicular to the foliation there is little or no shear wave splitting ($V_{S1} - V_{S2} < 0.05$ km/s [<~1%]).

4. Predicted Velocity Structure of the Exhuming PNG Terrane

4.1. Modeling Techniques

[21] To aid in the interpretation of seismological data from the area of the Papua New Guinea UHP terrane, we model the velocity structure of the exhuming terrane by extrapolating our CPO-derived seismic velocities to the pressures, temperatures and mineralogies expected at depth. To do so,

Table 4. Calculated Velocities Averaged Over the Three Thin Sections for Each Sample and Measured Velocities at 600 MPa[a]

	V_P					V_{S1}					V_{S2}				
	max	min	X	Y	Z	max	min	X	Y	Z	X	Y	Z	AV_P (%)	AV_S (%)
Calculated															
PNG/08-02	6.09	6.01	6.08	6.07	6.02	3.60	3.52	3.59	3.59	3.53	3.52	3.51	3.50	1.5	2.7
PNG/08-10	8.24	8.14	8.24	8.19	8.15	4.77	4.77	4.75	4.74	4.74	4.72	4.72	4.71	1.3	1.2
PNG/08-17	7.02	6.44	7.01	6.83	6.45	3.93	3.69	3.93	3.93	3.69	3.67	3.69	3.67	8.6	7.0
PNG/08-33	6.18	5.99	6.16	6.07	6.01	3.65	3.54	3.58	3.57	3.55	3.55	3.52	3.52	3.1	3.5
PNG/08-43	6.23	5.91	6.22	6.20	5.96	3.73	3.46	3.71	3.72	3.46	3.46	3.43	3.43	5.3	8.0
PNG/08-44	7.62	7.02	7.55	7.40	7.04	4.19	3.99	4.15	4.16	4.01	3.99	3.99	3.99	8.2	5.5
Measured															
PNG/08-02	6.10	5.96	5.96	6.02	6.10	3.66	3.29	3.52	3.66	3.29	3.45	3.43		2.3	6.6
PNG/08-10	8.20	7.70	8.20	7.79	7.70	4.63	4.41	4.63	4.62	4.41	4.56	4.51		6.3	2.4
PNG/08-17	6.95	6.35	6.95	6.94	6.35	4.24	3.78	4.08	4.24	3.78	4.16	3.96		9.0	7.0
PNG/08-33	6.23	5.87	6.23	6.01	5.87	3.89	3.34	3.89	3.48	3.34	3.79	3.43		6.0	2.8
PNG/08-43	6.44	5.93	6.44	6.27	5.93	3.91	3.51	3.91	3.82	3.51	3.81	3.72		8.3	2.7
PNG/08-44	7.58	7.17	7.58	7.17	7.32	4.41	4.09	4.41	4.09	4.23	4.13	4.23		5.6	6.6

[a]Maximum V_P (AV_P) and V_S (AV_S) anisotropies are also given.

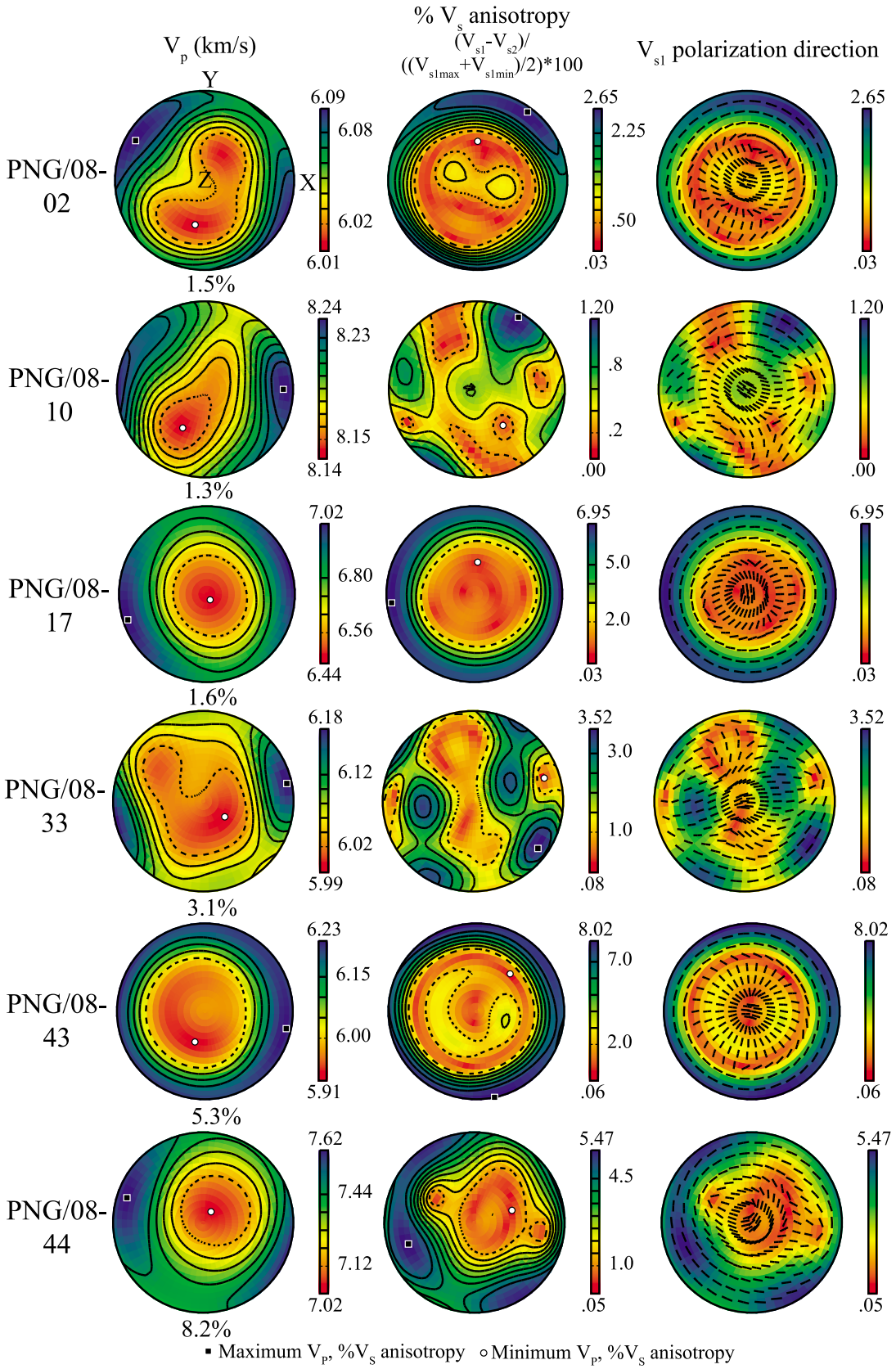

Figure 7. Lower hemisphere contour plots of V_P, V_S anisotropy, and V_{S1} polarization direction. The directions of the X, Y, and Z cores used for high-pressure velocity measurements are indicated in the top left plot. X is parallel to the lineation, and Z is perpendicular to the foliation. Percent V_P anisotropy is indicated below V_P plots.

Table 5. Bulk Compositions Based on EDS Analyses of Minerals and Mineral Proportions (Oxide wt %)

	SiO_2	TiO_2	Al_2O_3	FeO	MnO	MgO	CaO	Na_2O	K_2O	Total
PNG/08-02	73.8	0.1	15.5	0.8	0.0	0.3	2.9	5.8	0.4	99.6
PNG/08-10	52.6	1.8	15.6	11.9	0.2	5.9	7.1	4.8	0.1	99.9
PNG/08-17	56.6	0.5	14.2	9.1	0.1	6.7	9.1	3.3	0.2	99.7
PNG/08-33	75.2	0.1	14.3	0.9	0.0	0.5	1.0	5.1	2.6	99.7
PNG/08-43	73.6	0.3	12.4	2.9	0.2	2.3	2.1	3.5	2.3	99.7
PNG/08-44	46.1	0.7	15.3	11.6	0.1	9.3	13.6	2.3	0.8	99.7

we calculate the phase relations of rocks, and their isotropic velocities as a function of P and T based on the calculated phase relations.

[22] We calculated the phase relations of the rocks using Perple_X [*Connolly and Petrini*, 2002; *Connolly*, 2005] with bulk compositions (Table 5) determined from observed mineral compositions and modes. All the bulk compositions were simplified to the Na_2O–CaO–K_2O–MgO–FeO–MnO–Al_2O_3–TiO_2–SiO_2–H_2O system. The exclusion of some components (e.g., Cr) and the absence of some components from solid solution models (e.g., K_2O in amphibole) means that the calculations only approximate natural rocks and minerals. K_2O poses perhaps the greatest problem of this type because neglecting the presence of K_2O in amphibole means that the stability of K-white mica is overemphasized. For the gneisses, the dominant rock type, we calculated the phase relations using enough H_2O to stabilize the existing mineral assemblage (Table 6). We restricted our calculations to pressures of 0.5–3.5 GPa and temperatures of 500–800°C, conditions that cover the range expected. We use the well-tested activity models listed in Table 7.

Table 7. Perple_X Activity Models Used

Abbreviation	Mineral Solution	Model
Bio(HP)	biotite	*Powell and Holland* [1999]
F	fluid	*Connolly and Trommsdorff* [1991]
feldspar	feldspar	*Fuhrman and Lindsley*, 1988]
GlTrTsPg	Na-Ca amphibole	*Wei and Powell* [2003] and *White et al.* [2003]
Gt(HP)	garnet	*Holland and Powell* [1998]
O(HP)	olivine	*Holland and Powell* [1998]
Omph(HP)	clinopyroxene	*Holland and Powell* [1998]
Pheng(HP)	K-white mica	"parameters from Thermocalc"
San	K-feldspar	*Thompson and Hovis* [1979]

4.2. Modeling Results

[23] The three quartzofeldspathic gneisses (samples PNG/08-02, PNG/08-33, and PNG/08-43) have broadly similar pseudosections, with chiefly plagioclase + biotite assemblages at low pressure giving way to jadeite + quartz ± phengite ± zoisite at pressures above ~1.5 GPa at 700°C (Figure 8a). All three gneiss samples lack clinopyroxene and any evidence of former clinopyroxene, indicating that they either (1) did not equilibrate at eclogite-facies conditions or

Table 6. Perple_X Phase Relations (vol %) at 700°C and 0.5, 1, 1.5, 2.0, 2.5, 3, and 3.5 GPa[a]

	PNG02								PNG33								PNG43							
	Obs.	0.5	1.0	1.5	2.0	2.5	3.0	3.5	Obs.	0.5	1.0	1.5	2.0	2.5	3.0	3.5	Obs.	0.5	1.0	1.5	2.0	2.5	3.0	3.5
Quartz	30.5	32.8	32.3	32.4	48.5	48.5			31.2	34.0	33.8	33.3	46.7	46.8			36.0	41.2	40.9	41.1	48.1	47.4		
Coesite							46.4	46.8							44.3	44.3							45.0	45.1
Plagioclase	65.4	64.3	64.7	62.6					58.6	49.3	50.3	50.1					45.4	42.6	42.1	32.9				
K-feldspar					2.0	1.8	0.8			11.8	8.1	7.7	9.7	8.8	9.0	8.9		2.4	2.3	3.1	5.4	5.0	5.1	5.1
Biotite	3.8	1.6	1.2						3.4	3.8	3.2	1.9					9.9	13.4	13.5	7.6	2.0			
K-white mica				1.8	1.3	1.3	2.6	3.7	6.1		4.4	6.3	11.2	11.2	11.7	11.6				5.7	11.7	13.6	14.2	14.2
Amphibole				0.5													6.1							
Pyroxene					37.8	38.0	39.5	39.0					31.5	32.2	33.9	34.0				5.5	26.6	26.8	27.8	27.5
Garnet		0.8	1.3	2.4			1.9	4.0	0.6		0.1	0.7	0.9	0.8	0.6	0.4	2.5	0.1	0.9	4.0	6.0	6.9	7.6	8.0
H_2O		0.4	0.4	0.3																				
Ilmenite		0.1								0.1								0.3						
Rutile			0.1	0.1	0.1	0.1		0.1			0.1	0.1	0.1	0.1	0.1	0.1			0.1	0.2	0.2	0.2	0.2	0.2
Titanite							0.2												0.3					
Kyanite					3.8	3.8	4.2	4.2						0.1	0.5	0.8								
Sillimanite										1.1														
Lawsonite							0.3	0.2																
Zoisite	0.3				6.6	6.6	4.4	2.3																

	PNG17								PNG44								PNG10							
	Obs.	0.5	1.0	1.5	2.0	2.5	3.0	3.5	Obs.	0.5	1.0	1.5	2.0	2.5	3.0	3.5	Obs.	0.5	1.0	1.5	2.0	2.5	3.0	3.5
Quartz	11.6	6.1	10.2	18.2	18.9	18.0				6.3	12.4	17.0	16.0	13.5			5.7			1.4	8.5	8.5		
Coesite							16.6	16.6							12.4	12.4							7.7	7.7
Plagioclase	20.2	42.2	34.7							32.8	18.3							53.0	42.8	28.0				
Biotite		1.3	0.9	2.0	2.0					5.6	6.1	6.9	5.6					0.7	0.8	0.7	1.1	1.1	1.1	1.1
K-white mica						1.9	2.0	1.9	1.0				1.3	6.6	6.6	6.6	1.1						0.0	0.0
Amphibole	56.9	44.9	38.7	13.6					61.5	40.0	28.8	7.4						3.7	3.5	3.9	0.4			
Pyroxene			4.1	42.9	50.1	49.8	49.6	48.6	15.5	10.1	20.5	44.2	48.1	49.1	48.3	47.1	53.5	19.7	27.3	38.2	58.6	59.0	59.4	59.4
Garnet	0.3	4.7	10.0	20.7	25.6	27.1	28.7	29.8	3.9	4.5	12.6	22.0	26.1	28.1	29.9	31.2	37.7	15.8	23.3	26.4	29.8	29.8	30.1	30.1
H_2O		0.1	0.6	2.2	3.0	2.8	2.8	2.7			0.8	2.1	2.4	2.3	2.3	2.2					0.2	0.2	0.2	0.2
Ilmenite		0.6	0.6							0.7								2.2	2.3					
Rutile				0.4	0.4	0.4	0.4	0.4	0.1		0.4	0.5	0.5	0.5	0.5	0.5	1.8			1.4	1.5	1.5	1.5	1.5
Olivine																		5.0						
Zoisite	10.9								18.0								0.2							

[a]Obs, observed modal proportions.

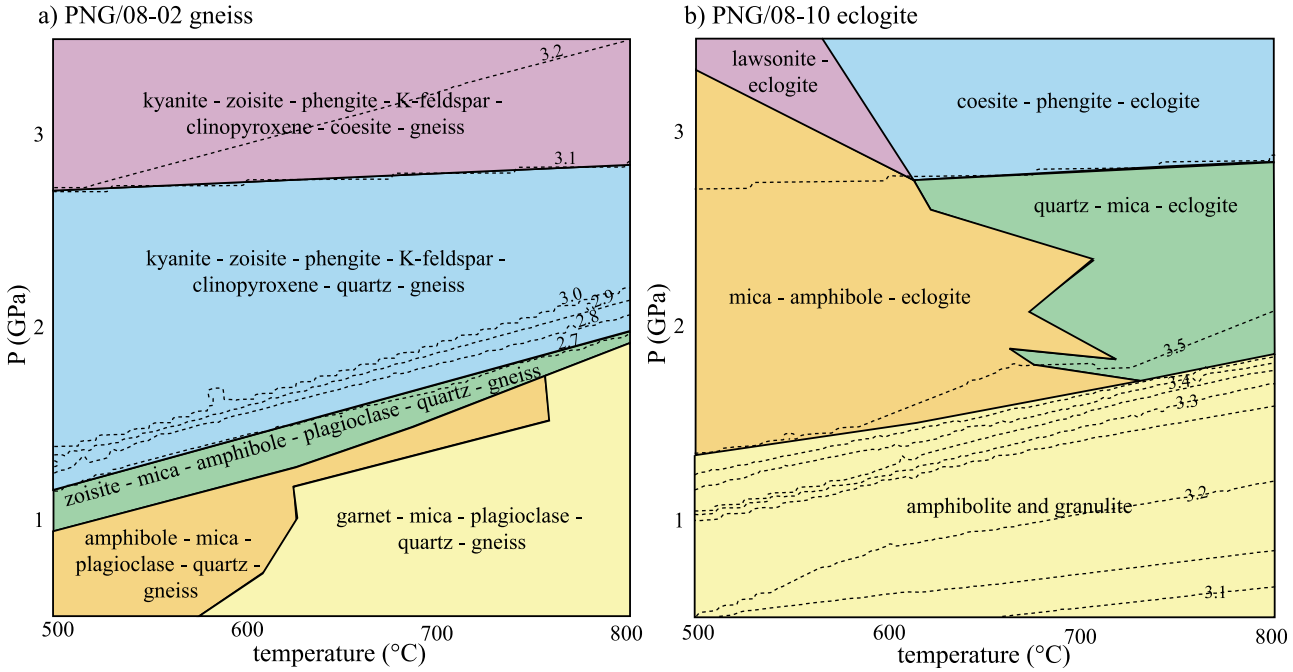

Figure 8. Pseudosections for (a) PNG-02, a typical gneiss pseudosection, and (b) PNG-10, an eclogite pseudosection. The amphibolites have pseudosections similar to the eclogite. Dashed contours are density (g/cm^3).

(2) did, and were subsequently thoroughly overprinted; this issue is typical of UHP terranes [*Peterman et al.*, 2009]. The presence of relict clinozoisite in gneiss sample PNG/08-02 indicates equilibration at pressures of ≥1.5 GPa at 700°C.

[24] The three mafic rocks modeled, the eclogite sample PNG/08-10 and amphibolite samples PNG/08-17 and PNG/08-44, have rather similar phase relations, with plagioclase breaking down to eclogite-facies mineral assemblages at ~1.6 GPa at 700°C (Figure 8b). Interestingly, amphibole is calculated to be stable to higher pressure in the eclogite than in the amphibolites, but this is consonant with the metamorphic texture of the rock, which shows that this is one of those unusual eclogites that contains amphibole in the coesite stability field [*Chopin and Sobolev*, 1995]. The mica calculated to be present in the amphibolites is an artifact of the amphibole activity model, which lacks K_2O, and should be ignored. The pseudosection indicates that the phases in the eclogite, which lacks biotite, recrystallized at <700°C. The pseudosection suggests that the peak P phases in amphibolite PNG/08-17 recrystallized around 500–600°C and 1–2 GPa and were overprinted at 500–700°C and ~1 GPa. Likewise, the peak P phases in amphibolite PNG/08-44 apparently recrystallized around 500–600°C and 1.3–1.7 GPa and were overprinted at 500–650°C and ~1 GPa.

[25] To model the velocity structure of the Papua New Guinea UHP terrane at depth, we use the mineralogy predicted for the various rocks at pressures of 0.5–3.5 GPa in 0.25 GPa increments, all at 700°C (varying the temperature by 200°C results in <6% change in calculated velocities). The velocity at the surface is modeled using the phases present in our samples. We calculate the isotropic velocities using the *Hacker and Abers* [2004] Excel macro with mineral assemblages predicted by Perple_X. The isotropic velocities can be directly compared with published seismic velocity models [*Ferris et al.*, 2006]. The *isotropic* velocities calculated for each rock composition are listed in Table 8. The velocities decrease by ~3–5% for the gneisses, and ~6–12% for the amphibolites and eclogite from STP to 700°C and 0.5 GPa, and then increase with increasing pressure to a maximum of 8.2 km/s for the amphibolites (PNG/08-17 and PNG/08-44) and eclogite (PNG/08-10) at 3 GPa. The large velocity decrease in the amphibolites and eclogite from STP

Table 8. Isotropic Velocities (km/s) for Each Modeled Rock Calculated at STP and 700°C Using the Data of *Hacker and Abers* [2004]

	STP	0.5 GPa	1 GPa	1.5 GPa	2 GPa	2.5 GPa	3 GPa
				Quartzofeldspathic Gneiss			
PNG/08-02							
V_P	6.2	6.0	6.1	6.3	6.9	6.9	8.1
V_S	3.8	3.6	3.7	3.8	4.3	4.3	4.6
PNG/08-33							
V_P	6.2	5.9	6.0	6.1	6.6	6.6	7.7
V_S	3.8	3.6	3.6	3.7	4.1	4.1	4.4
PNG/08-43							
V_P	6.1	5.8	5.9	6.1	6.5	6.6	7.7
V_S	3.7	3.5	3.6	3.7	4.0	4.1	4.4
				Amphibolite			
PNG/08-17							
V_P	6.8	6.4	6.6	7.3	7.5	7.6	8.2
V_S	4.0	3.6	3.8	4.3	4.4	4.5	4.6
PNG/08-44							
V_P	7.3	6.5	6.7	7.2	7.4	7.6	8.0
V_S	4.2	3.7	3.9	4.2	4.3	4.4	4.5
				Eclogite			
PNG/08-10							
V_P	7.8	6.8	7.1	7.4	7.9	7.9	8.2
V_S	4.5	3.8	4.0	4.2	4.5	4.6	4.6

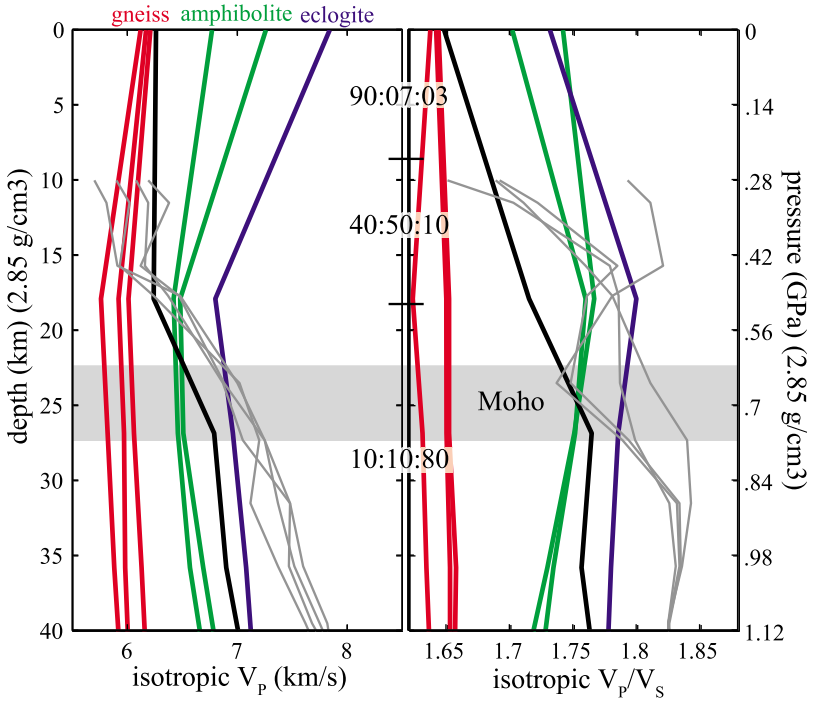

Figure 9. Velocity profile of *Ferris et al.* [2006] (gray lines) requires increasing abundance of mafic rocks with depth. Isotropic velocities for PNG gneisses (red), amphibolites (green), and eclogite (blue) calculated at 700°C using the method of *Hacker and Abers* [2004] using mineral proportions predicted by Perple_X. Black represents a mixed terrane of gneiss:amphibolite:eclogite mixed in the proportions indicated.

to 700°C and 0.5 GPa is due to incomplete retrograde metamorphism; specifically, the predicted mineral assemblages at 700°C and 0.5 GPa for all 3 mafic compositions includes at least 30 vol % plagioclase, whereas PNG/08-17 is the only mafic sample to contain measurable plagioclase (~20 vol %).

4.3. Comparison With Seismic Observations

[26] The *isotropic* velocities may be directly compared with seismic measurements of crustal velocity. The crustal section of *Ferris et al.* [2006] below Fergusson Island has velocities that increase from ~6 km/s at 10 km depth to ~8 km/s at 40 km depth (Figure 9). The calculated velocities for the modeled PNG rocks at depth are plotted in Figure 9. At the surface, the PNG terrane is mostly quartzofeldpathic gneiss, with minor amphibolite and eclogite. A terrane of dominantly quartzofeldspathic rocks does not match the observed seismic velocities at depth; however, a good match can be achieved if the bulk composition of the terrane shifts toward that of the eclogite at depths of ~20 km. The black line in Figure 9 shows the velocity calculated for a mixed terrane composed of (gneiss:amphibolite:eclogite) 90:07:03 at the surface, 40:50:10 at 0.5 GPa, 10:10:80 from 0.75 to 1 GPa, and 00:10:90 below 1.25 GPa. The addition of up to 40% granodiorite decreases the velocities toward that of the gneiss because both rocks are quartzofeldspathic. The seismic Moho is at ~23 km below Fergusson Island, and ~28 km depth below Goodenough Island, so it is not surprising that none of the rock compositions currently at the surface have velocities that match those observed below the Moho.

[27] Based on our calculations of seismic anisotropy of surface samples from CPO measurements, we expect the anisotropy at depth in the PNG terrane to be related to the rock fabric; specifically, we expect the slow axis of anisotropy to be perpendicular to the foliation. For example, if the terrane is exhuming as a diapiric sheet [*Little et al.*, 2011], with gently dipping foliations at Earth's surface and near-vertical foliations at depth, the slow axis of anisotropy should change downward from vertical to horizontal. If the terrane is exhuming as an axially symmetric diapir with a constrictional flow field, we expect a vertically plunging unique fast axis of anisotropy. If the terrane is exhuming as a slab by reversal of slip along the original subduction interface [*Webb et al.*, 2008], we expect the unique slow axis of anisotropy to be orthogonal to the slab.

[28] Measurements of the seismic anisotropy of the PNG terrane are currently being made, and as yet there are no published seismic measurements with which to compare our calculations. Unlike other measured crustal sections [*Sherrington et al.*, 2004; *Ozacar and Zandt*, 2004; *Porter et al.*, 2011], the PNG UHP terrane at the surface is remarkably isotropic and will produce relatively minor S wave splitting. For example, if the UHP terrane is ~40 km thick, homogeneous, and composed dominantly of gneiss with vertical foliation (resulting in maximum shear wave splitting) it will contribute only ~0.3 s to the shear wave splitting of vertically incident waves. Of the three rock types at the surface, the amphibolite is the most anisotropic, but with increasing pressure amphibole converts to a garnet + pyroxene assemblage, which has a lower anisotropy than

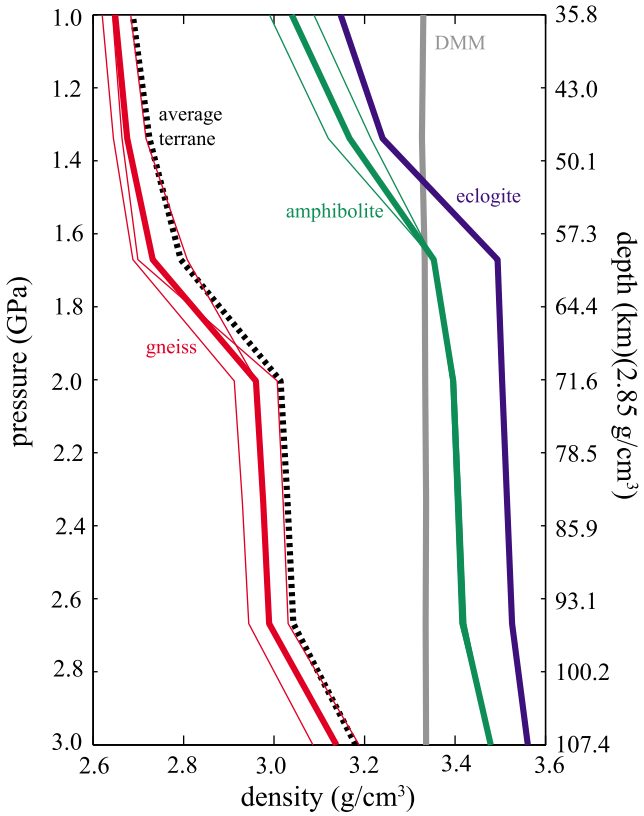

Figure 10. The exhuming quartzofeldpathic terrane is buoyant below depleted MORB mantle (DMM) down to 3 GPa. Density for the PNG gneisses (red), amphibolites (green), and eclogite (blue). Averages represented by thick lines. Average terrane (dashed black) is for the proportions currently at the surface, 90:07:03 (gneiss:amphibolite: eclogite). DMM shown in gray.

the surface mineral assemblage due to the increase in isotropic garnet. If the PNG terrane below 20 km is indeed mostly eclogite as suggested by the isotropic velocities, the seismic anisotropy is expected to be extremely low, ~1%, and likely impossible to measure using current methods.

5. Predicted Density Structure of the Exhuming PNG Terrane

[29] To understand the density structure of the exhuming PNG terrane, we calculate the phase relations and densities of rocks using Perple_X at various pressures during isothermal compression at 700°C. Varying the temperature from 500 to 800°C results in less than 2% change in the densities calculated. The densities of all 3 gneisses at 700°C down to 3 GPa are significantly lower than that of MORB-depleted mantle (DMM) for a standard mantle adiabat (Figure 10). The amphibolites and the eclogite become more dense than DMM at ~1.6 and 1.4 GPa, respectively. An average PNG terrane composed of 90% gneiss and 10% mafic rock (dashed black line in Figure 10) is more buoyant than DMM at all depths. For the PNG terrane to be more buoyant than DMM at depth it must consist of >60% quartzofeldspathic gneiss. The velocity model of *Ferris et al.* [2006] suggests that the current PNG terrane at depth is likely to contain more than 50% mafic rocks at depths greater than ~20 km (Figure 9).

6. Conclusions

[30] High pressure laboratory measurements of seismic velocities from the Papua New Guinea ultrahigh-pressure terrane give V_P of 5.8–6.3 km/s for gneiss, 6.5–7.7 km/s for amphibolite, and 7.7–8.2 km/s for eclogite, and V_S of 3.4–3.9 km/s for gneiss, 4.0–4.4 km/s for amphibolite, and 4.5–4.6 km/s for eclogite. Seismic velocities calculated from EBSD measurements are within 5% of the measured velocities. Seismic anisotropy is low in the PNG terrane, and ranges from 2 to 9% in V_P, and 2–7% in V_S, and is highest in rocks containing abundant strongly oriented hornblende (i.e., amphibolite). The calculated shear wave splitting perpendicular to the flow plane is minimal, <1%.

[31] The orientation of seismic anisotropy is controlled by the orientation of the foliation, or flow plane in the rock. For an exhuming diapiric sheet, a change in the unique axis of anisotropy would be expected across the diapir. In contrast to the subduction inversion model with near horizontal foliation throughout, for which our calculations would suggest no changes in crustal anisotropy. Comparison of the crustal velocity model of *Ferris et al.* [2006] and our calculations suggests that the material below ~20 km depth is mostly mafic. Our calculations suggest very weak (~3–4% in V_P and V_S) anisotropy; however, if observed, the pattern of the seismic anisotropy in the PNG terrane may be used to test hypotheses about how UHP terranes are exhumed.

[32] **Acknowledgments.** Thoughtful and constructive reviews from Phil Skemer and an anonymous reviewer improved this manuscript. This work was funded by NSF grant EAR-0607775.

References

Aleksandrov, K. S., and T. V. Ryzhova (1961), The elastic properties of rock-forming minerals: II layered silicates, *Izv. Acad. Sci. USSR Phys. Solid Earth*, Engl. Transl., no. 11, 1165–1168.

Baldwin, S. L., B. D. Monteleone, L. E. Webb, P. G. Fitzgerald, M. Grove, and E. J. Hill (2004), Pliocene eclogite exhumation at plate tectonic rates in eastern Papua New Guinea, *Nature*, *431*, 263–267, doi:10.1038/nature02846.

Baldwin, S. L., L. E. Webb, and B. D. Monteleone (2008), Late Miocene coesite-eclogite exhumed in the Woodlark Rift, *Geology*, *36*, 735–738, doi:10.1130/G25144A.1.

Bascou, J., A. Tommasi, and D. Mainprice (2002), Plastic deformation and development of clinopyroxene lattice preferred orientations in eclogites, *J. Struct. Geol.*, *24*, 1357–1368, doi:10.1016/S0191-8141(01)00137-7.

Bass, J. D. (1995), Elasticity of minerals, glasses, and melts, in *Mineral Physics and Crystallography: A Handbook of Physical Constants*, *AGU Ref. Shelf*, vol. 2, edited by T. J. Ahrens, pp. 45–63, AGU, Washington, D. C.

Bhagat, S. S., J. D. Bass, and J. R. Smyth (1992), Single-crystal elastic properties of omphacite-C2/c by Brillouin spectroscopy, *J. Geophys. Res.*, *97*, 6843–6848, doi:10.1029/92JB00030.

Birch, F. (1960), The velocity of compressional waves in rocks to 10 kilobars, part 1, *J. Geophys. Res.*, *65*, 1083–1102, doi:10.1029/JZ065i004p01083.

Chopin, C. (1984), Coesite and pure pyrope in high-grade blueschists of the western Alps: A first record and some consequences, *Contrib. Mineral. Petrol.*, *86*, 107–118, doi:10.1007/BF00381838.

Chopin, C., and N. V. Sobolev (1995), Principal mineralogic indicators of UHP in crustal rocks, in *Ultrahigh Pressure Metamorphism*, edited by R. G. Coleman and X. Wang, pp. 96–131, Cambridge Univ. Press, Cambridge, doi:10.1017/CBO9780511573088.004.

Christensen, N. I. (1965), Compressional wave velocities in metamorphic rocks at pressures to 10 kilobars, *J. Geophys. Res.*, *70*, 6147–6164, doi:10.1029/JZ070i024p06147.

Collins, M. D., and J. M. Brown (1998), Elasticity of an upper mantle pyroxene, *Phys. Chem. Miner.*, *26*, 7–13, doi:10.1007/s002690050156.

Connolly, J. A. D. (2005), Computation of phase equilibria by linear programming: A tool for geodynamic modeling and its application to subduction zone decarbonation, *Earth Planet. Sci. Lett.*, *236*, 524–541, doi:10.1016/j.epsl.2005.04.033.

Connolly, J. A. D., and K. Petrini (2002), An automated strategy for calculation of phase diagram sections and retrieval of rock properties as a function of physical conditions, *J. Metamorph. Geol.*, *20*, 697–708, doi:10.1046/j.1525-1314.2002.00398.x.

Connolly, J. A. D., and V. Trommsdorff (1991), Petrogenetic grids for metacarbonate rocks: Pressure-temperature phase-diagram projection for mixed-volatile systems, *Contrib. Mineral. Petrol.*, *108*, 93–105, doi:10.1007/BF00307329.

Davies, H. L., and R. G. Warren (1992), Eclogites of the D'Entrecasteaux Islands, *Contrib. Mineral. Petrol.*, *112*, 463–474, doi:10.1007/BF00310778.

Ferris, A., G. A. Abers, B. Zelt, B. Taylor, and S. Roecker (2006), Crustal structure across the transition from rifting to spreading: The Woodlark rift system of Papua New Guinea, *Geophys. J. Int.*, *166*, 622–634, doi:10.1111/j.1365-246X.2006.02970.x.

Fuhrman, M. L., and D. H. Lindsley (1988), Ternary-feldspar modeling and thermometry, *Am. Mineral.*, *73*, 201–215.

Godfrey, N. J., N. I. Christensen, and D. A. Okaya (2000), Anisotropy of schists: Contribution of crustal anisotropy to active source seismic experiments and shear-wave splitting observations, *J. Geophys. Res.*, *105*, 27,991–28,007, doi:10.1029/2000JB900286.

Hacker, B. R., and G. A. Abers (2004), Subduction factory 3: An Excel worksheet and macro for calculating the densities, seismic wave speeds, and H_2O contents of minerals and rocks at pressure and temperature, *Geochem. Geophys. Geosyst.*, *5*, Q01005, doi:10.1029/2003GC000614.

Hacker, B. R., and J. M. Christie (1990), Brittle/ductile and plastic/cataclastic transitions in experimentally deformed and metamorphosed amphibolite, in *The Brittle-Ductile Transition in Rocks*, *Geophys. Monogr. Ser.*, vol. 56, edited by A. G. Duba et al., pp. 127–147, AGU, Washington, D. C.

Hacker, B. R., and S. M. Peacock (1995), Creation, preservation, and exhumation of coesite-bearing, ultrahigh-pressure metamorphic rocks, in *Ultrahigh Pressure Metamorphism*, edited by R. G. Coleman and X. Wang, pp. 159–181, Cambridge Univ. Press, Cambridge, U. K., doi:10.1017/CBO9780511573088.006.

Hacker, B. R., L. Ratschbacher, L. E. Webb, M. McWilliams, T. R. Ireland, A. Calvert, S. Dong, H.-R. Wenk, and D. Chateigner (2000), Exhumation of ultrahigh-pressure continental crust in east central China: Late Triassic–Early Jurassic tectonic unroofing, *J. Geophys. Res.*, *105*, 13,339–13,364, doi:10.1029/2000JB900039.

Hacker, B. R., T. B. Andersen, S. Johnston, A. R. C. Kylander-Clark, E. Peterman, E. O. Walsh, and D. Young (2010), High-temperature deformation during continental-margin subduction & exhumation: The ultrahigh-pressure Western Gneiss Region of Norway, *Tectonophysics*, *480*, 149–171, doi:10.1016/j.tecto.2009.08.012.

Hill, E. J. (1994), Geometry and kinematics of shear zones formed during continental extension in eastern Papua New Guinea, *J. Struct. Geol.*, *16*, 1093–1105, doi:10.1016/0191-8141(94)90054-X.

Hill, E. J., and S. L. Baldwin (1993), Exhumation of high-pressure metamorphic rocks during crustal extension in the D'Entrecasteaux region, Papua New Guinea, *J. Metamorph. Geol.*, *11*, 261–277, doi:10.1111/j.1525-1314.1993.tb00146.x.

Holland, T. J. B., and R. Powell (1998), An internally consistent thermodynamic data set for phases of petrological interest, *J. Metamorph. Geol.*, *16*, 309–343, doi:10.1111/j.1525-1314.1998.00140.x.

Kretz, R. (1983), Symbols for rock-forming minerals, *Am. Mineral.*, *68*, 277–279.

Lakshtanov, D. L., S. V. Seinogeikin, and J. D. Bass (2007), High-temperature phase transitions and elasticity of silica polymorphs, *Phys. Chem. Miner.*, *34*, 11–22, doi:10.1007/s00269-006-0113-y.

Le Roux, V., A. Tommasi, and A. Vauchez (2008), Feedback between melt percolation and deformation in an exhumed lithosphere-asthenosphere boundary, *Earth Planet. Sci. Lett.*, *274*, 401–413, doi:10.1016/j.epsl.2008.07.053.

Linker, M. F., S. H. Kirby, A. Ord, and J. M. Christie (1984), Effects of compression direction on plasticity and rheology of hydrolytically weakened synthetic quartz at atmospheric pressure, *J. Geophys. Res.*, *89*, 4241–4255, doi:10.1029/JB089iB06p04241.

Lister, G. S. (1979), Fabric transitions in plastically deformed quartzites: Competition between basal, prism and rhomb systems, *Bull. Mineral.*, *102*, 232–241.

Little, T. A., B. R. Hacker, S. M. Gordon, S. L. Baldwin, P. G. Fitzgerald, S. Ellis, and M. Korchinski (2011), Diapiric exhumation of Earth's youngest (UHP) eclogites in the gneiss domes of the D'Entrecasteaux Islands, Papua New Guinea, *Tectonophysics*, doi:10.1016/j.tecto.2011.06.006, in press.

Lloyd, G. E., R. W. H. Butler, M. Casey, and D. Mainprice (2009), Mica, deformation fabrics and the seismic properties of the continental crust, *Earth Planet. Sci. Lett.*, *288*, 320–328, doi:10.1016/j.epsl.2009.09.035.

Mainprice, D. A. (1990), FORTRAN program to calculate seismic anisotropy from the lattice preferred orientation of minerals, *Comput. Geosci.*, *16*, 385–393, doi:10.1016/0098-3004(90)90072-2.

Mao, Z., F. M. Jiang, and T. S. Duffy (2007), Single crystal elasticity of zoisite $Ca_2Al_3Si_3O_{12}(OH)$ by Brillouin scattering, *Am. Mineral.*, *92*, 570–576, doi:10.2138/am.2007.2329.

Monteleone, B. D., S. L. Baldwin, L. E. Webb, P. G. Fitzgerald, M. Grove, and A. K. Schmitt (2007), Late Miocene-Pliocene eclogite facies metamorphism, D'Entrecasteaux Islands, SE Papua New Guinea, *J. Metamorph. Geol.*, *25*, 245–265, doi:10.1111/j.1525-1314.2006.00685.x.

Ozacar, A. A., and G. Zandt (2004), Crustal seismic anisotropy in central Tibet: Implications for deformational style and flow in the crust, *Geophys. Res. Lett.*, *31*, L23601, doi:10.1029/2004GL021096.

Peterman, E. M., B. R. Hacker, and E. F. Baxter (2009), Phase transformations of continental crust during subduction and exhumation: Western Gneiss Region, Norway, *Eur. J. Mineral.*, *21*, 1097–1118, doi:10.1127/0935-1221/2009/0021-1988.

Porter, R., G. Zandt, and N. McQuarrie (2011), Pervasive lower crustal seismic anisotropy in southern California: Evidence for underplated schists, *Lithopshere*, doi:10.1130/L126.1, in press.

Powell, R., and T. Holland (1999), Relating formulations of the thermodynamics of mineral solid solutions; activity modeling of pyroxenes, amphiboles, and micas, *Am. Mineral.*, *84*, 1–14.

Ryzhova, T. V. (1964), Elastic properties of plagioclase, *Izv. Geophys. Ser.*, *7*, 1049–1051.

Sherrington, H. F., G. Zandt, and A. Frederiksen (2004), Crustal fabric in the Tibetan Plateau based on waveform inversions for seismic anisotropy parameters, *J. Geophys. Res.*, *109*, B02312, doi:10.1029/2002JB002345.

Soga, N. (1967), Elastic constants of garnet under pressure and temperature, *J. Geophys. Res.*, *72*, 4227–4234, doi:10.1029/JZ072i016p04227.

Tatham, D. J., G. E. Lloyd, R. W. H. Butler, and M. Casey (2008), Amphibole and lower crustal seismic properties, *Earth Planet. Sci. Lett.*, *267*, 118–128, doi:10.1016/j.epsl.2007.11.042.

Thompson, J. B., and G. L. Hovis (1979), Entropy of mixing in sanidine, *Am. Mineral.*, *64*, 57–65.

Vaughan, M. T., and S. Guggenheim (1986), Elasticity of muscovite and its relation to crystal structure, *J. Geophys. Res.*, *91*, 4657–4664, doi:10.1029/JB091iB05p04657.

Wang, X., J. G. Liou, and H. K. Mao (1989), Coesite-bearing eclogite from the Dabie Mountains in central China, *Geology*, *17*, 1085–1088, doi:10.1130/0091-7613(1989)017<1085:CBEFTD>2.3.CO;2.

Webb, L. E., S. L. Baldwin, T. A. Little, and P. G. Fitzgerald (2008), Can microplate rotation drive subduction inversion?, *Geology*, *36*, 823–826, doi:10.1130/G25134A.1.

Wei, C., and R. Powell (2003), Phase relations in high-pressure metapelites in the system KFMASH (K_2O-FeO-MgO-Al_2O_3-SiO_2–H_2O) with application to natural rocks, *Contrib. Mineral. Petrol.*, *145*, 301–315, doi:10.1007/s00410-003-0454-1.

White, R. W., R. Powell, and G. N. Phillips (2003), A mineral equilibria study of the hydrothermal alteration in mafic greenschist facies rocks at Kalgoorlie, Western Australia, *J. Metamorph. Geol.*, *21*, 455–468, doi:10.1046/j.1525-1314.2003.00454.x.

G. A. Abers, Lamont-Doherty Earth Observatory, Columbia University, 61 Route 9W, Seismology Bldg., Rm. 108, Palisades, NY 10964, USA.

S. L. Baldwin, Department of Earth Sciences, Syracuse University, Syracuse, NY 13244, USA.

S. J. Brownlee and B. R. Hacker, Earth Research Institute, University of California, 1006 Webb Hall, MC 9630, Santa Barbara, CA 93106-3060, USA. (sbrownlee@eri.ucsb.edu)

T. A. Little, Department of Earth Sciences, Victoria University of Wellington, PO Box 600, Wellington 6140, New Zealand.

M. Salisbury, Geological Survey of Canada-Atlantic, Bedford Institute of Oceanography, PO Box 1006, Dartmouth, NS B2Y 4A2, Canada.

G. Seward, Department of Earth Science, University of California, Santa Barbara, CA 93106-9630, USA.